



GFRP APPLIED TO CAPACITOR BANK STRUCTURES OF ELECTRIC ENERGY SUBSTATIONS

Marcos W. Souza*, Carlos A. Cimini Jr.*

*UFMG – Federal University of Minas Gerais, Brazil

Keywords: *GFRP, pultruded bars, capacitor bank, electrical energy substations*

Abstract

In this work, an alternative capacitor bank framed structure was designed using GFRP pultruded bars. A finite element model was developed to simulate the structure static behavior and stability. Material properties were evaluated by a characterization test program. A prototype of the structure was built, instrumented and tested in order to validate the model. Although test was interrupted by system malfunction, results fairly agreed with model predictions. Additional three critical load cases were simulated. Results of these simulations showed large safety margins for static analysis. However, safety margins for global stability were marginal, indicating that the structure should be reinforced in some points. In general, results support the use of GFRP as an alternative material in the design of capacitor bank framed structures.

1 Introduction

The use of composite materials in infrastructure applications has increased in the last decades [1]. However, specific applications are not trivial, requiring more than simple stress analysis and design. Understanding well the nature of the loading system and the environment in which the structure will operate is mandatory to achieve a successful design.

Among all structures of electric energy substations, capacitor banks are more susceptible to be involved in electric accidents. Often reported, these accidents mainly involve animals such as squirrels, birds or possums, as these substations are located on the outskirts of the urban centers. Human accidents, although rare, may also occur and have a higher level of impact. Short-circuits and weather conditions can also be cause of accidents. These occurrences may result in local power outage with restricted effects, but also may produce a cascading

failure effect on the electrical network, leading to more severe blackouts.

Composite materials are ideal to be used in the design of electric-system structures, especially glass fiber reinforced plastics (GFRP). Its dielectric properties added to low weight and relative low cost of automated manufacture processes, such as pultrusion [2], makes it an excellent candidate to compete with materials traditionally used, such as steel or concrete. The insulation characteristics of GFRP increase the safety level of the installation concerning the risk of electric accidents, which is a desirable feature for this kind of design. Protecting the structure for atmospheric electric discharges is an additional concern, since GFRP is an insulating material.

However, designers of structures of electric substations are more cautious when designing for stiffness and/or strength failures, and tend to be conservative on the use of new materials as well as of new design concepts. Therefore, keeping the geometry limited to frame-like structure concept would be desirable to minimize the impact of introducing a new alternative material. This concept is also adequate for the use of GFRP pultruded bars.

As for the frame bar connections, bolted joints presented the simplest design concept and therefore are more suitable for the proposed conservative design [3].

Designers are also aware that both static behavior as well as the stability of the structure should be analyzed for the critical load cases.

In this work, an alternative capacitor bank structure was designed using GFRP in the form of a frame composed by pultruded bars. Bars were connected with bolts. A finite element model was developed to simulate the structure static behavior and stability. A test prototype of the designed structure was later manufactured, instrumented with strain gages and tested in order to verify the design and the viability of this alternative application.

2 Methodology

2.1 Material Characterization

In order to assemble the test prototype structure, pultruded L (50.8mm x 50.8mm x 6.35mm = 2" x 2" x 1/4") and U (28.6mm x 28.6mm x 101.6mm x 6.35mm = 1 1/8" x 1 1/8" x 4" x 1/4") shaped profiles were used. These profiles, named PullPlast 525 series, were manufactured by Webber Pultruded Profiles (WPP) using glass fibers embedded in an isophthalic polyester resin with ultraviolet inhibitor and fire retardant additive.

Material characterization was performed in test specimens taken from the pultruded bars, both in the fibers and perpendicular to the fibers directions.

Specimens were instrumented with strain gages on the longitudinal and transverse directions, in order to evaluate the Young's Modulus, Poisson's Ratio and Tensile Strength.

Standard tensile testing [4] was conducted on the test specimens and results were used to feed the finite element analysis of the structure.

2.2 Definition of the Structure Geometry

A specific capacitor bank was selected to verify the design using GFRP (Fig. 1). This structure was a traditional modular framed structure used by energy companies in electric substations. It consists of a two-bay truss separated by glass insulators. The lower bay is designed to comply with the height restraints for electric substations, which are related to workers and vehicles operating nearby. The upper bay, divided into three stores, is responsible to house the capacitors (up to five per store). On the top of the superior bay are located the energy busbars which are responsible for the electrical connections between the capacitor bank and the substation electrical system. Upper case letters were used to depict global coordinate system axes X, Y and Z.

2.3 Loads in the Capacitor Bank

The loads acting in the structure can be divided into three basic categories: weight loads (capacitors and structure), wind loads and short-circuit electromagnetic loads.

2.3.1 Weight Loads

Capacitors are generally heavy due to insulating oil enclosed within their structure. Therefore, the weight of capacitors should be considered as a dead load on the structural analysis. A single concentrated load was used to represent

each capacitor weight applied on the projection point of its center of gravity on the store frontal bar.

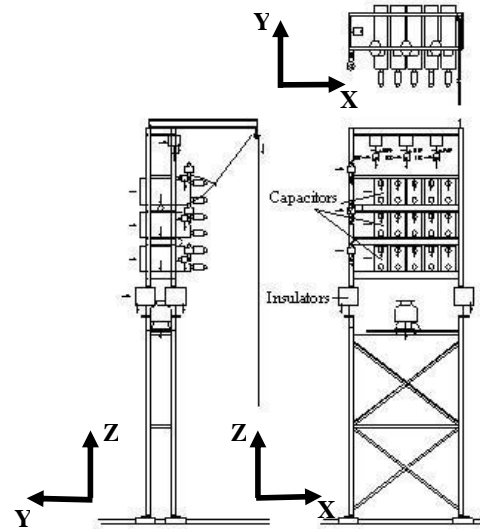


Fig. 1. Capacitor bank structure

2.3.2 Wind Loads

The basic equations used in the calculation of the wind loads are given by Eqs. 1 to 6 [5]. This calculation was divided into the six following steps.

(a) project wind velocity (Eq. 1)[5]:

$$V_p = K_r K_d \left(\frac{H}{10} \right)^{\frac{1}{n}} V_T \quad (1)$$

where:

V_p : project wind velocity [m/s];

K_r : non-dimensional tabled ground roughness coefficient varying from 0.67 to 1.08;

K_d : non-dimensional tabled time conversion coefficient for wind velocities with different integration times varying from 0.8 to 1.9;

H : structure height [m];

n : non-dimensional tabled constant dependent of the ground roughness and time integration, varying from 8 to 13;

V_T : wind velocity for a period of 50 years [m/s].

(b) air specific mass (Eq. 2)[5]:

$$\rho = \frac{1,293}{1 + 0,00367.t_c} \left(\frac{16000 + 64.t_c - ALT}{16000 + 64.t_c + ALT} \right) \quad (2)$$

where:

ρ : air specific mass [kg/m³];

t_c : average temperature at the location [°C];

ALT : altitude at the location [m].

(c) wind dynamic pressure (Eq. 3)[5]:

$$q_o = \frac{1}{2} \rho V_p^2 \quad (3)$$

where:

q_o : reference dynamic pressure [N/m²];
 V_p : project wind velocity [m/s];
 ρ : air specific mass [kg/m³].

(d) wind forces acting on accessories (Eq. 4)[5]:

$$A_i = q_o \cdot C_{xi} \cdot S_i \quad (4)$$

where:

A_i : wind force acting on the accessory i [N];
 q_o : reference dynamic pressure [N/m²];
 C_{xi} : non-dimensional drag coefficient of accessory i ;
 S_i : orthogonal projected area of accessory i [m²].

(e) wind forces acting on the structure (Eq. 5)[5]:

$$A_t = q_o (1 + 0,2 \cdot \sin^2 2\theta) (S_{T1} \cdot C_{XT1} \cdot \sin^2 \theta + S_{T2} \cdot C_{XT2} \cdot \cos^2 \theta) \quad (5)$$

where:

A_t : wind force acting on the support t [N];
 q_o : reference dynamic pressure [N/m²];
 θ : wind incidence angle [rad];
 S_{T1} , S_{T2} : total projected effective area for faces 1 and 2 of support t , respectively [m²];
 C_{XT1} , C_{XT2} : non-dimensional tabled structure drag coefficient for faces 1 and 2 of support t , respectively.

Note that for the structure elements (pultruded bars), there are two wind incidence faces of the square cross section, with respective projected areas and drag coefficients.

(f) wind forces acting in the busbar (Eq. 6)[5]:

$$A_c = q_o C_{xc} \alpha d \frac{Z}{2} \sin^2 \theta \quad (6)$$

where:

q_o : reference dynamic pressure [N/m²];
 C_{xc} : non-dimensional busbar drag coefficient;
 α : non-dimensional tabled effectiveness factor;
 d : busbar diameter [m];
 Z : busbar span length [m];
 θ : wind incidence angle [rad].

2.3.3 Short-circuit electromagnetic Loads

In the moment of the short-circuit accident, the current reaches the values equivalent to $(2\sqrt{2})I_{cc}$ in which I_{cc} indicates the effective current value for the short-circuit in amperes [6][7][8]. Interaction

forces then appear between the conductors, which can be attraction or repulsion forces, depending on the direction of the currents. Therefore, three cases of short-circuit were studied for a three-phase electrical system, according to the directions of the currents in each phase. These cases, respectively named load cases 1, 2 and 3, are shown on Figs. 2, 3 and 4.

The basic equation used in the calculation of the short-circuit electromagnetic loads was Eq. 7 [6].

$$\frac{F}{L} = \frac{\mu_0 I I'}{2\pi d} \quad (7)$$

where:

F/L : magnetic force between busbars [N/m];
 μ_0 : air magnetic permeability [H.m⁻¹];
 I and I' : current in adjacent busbars [A];
 d : distance between the busbars [m].

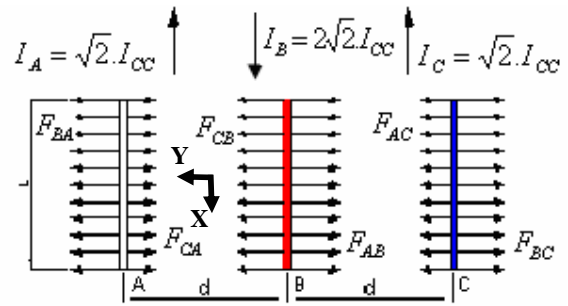


Fig. 2. Representation of case 1 short-circuit

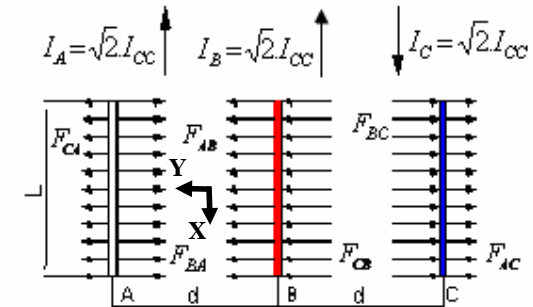


Fig. 3. Representation of case 2 short-circuit

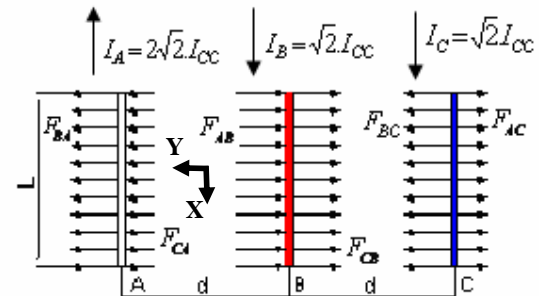


Fig. 4. Representation of case 3 short-circuit

2.4 Finite Element Model

A finite element model was developed using ANSYS 5.7 finite element platform. Beam elements (BEAM 189-3D) were used for in order to allow distributing capacitor weight, short-circuit and wind loads and also to allow moments to be transferred at the joints. Rigid elements were used to simulate the insulators between the lower and upper bays. The structure was clamped on the four points contacting the ground.

Beam element local coordinate system is shown in Fig. 5. Longitudinal x-axis is aligned with member axis while transverse y-axis and z-axis define the cross section. Lower case letters were used to depict local coordinate system axes x, y and z, for the beam elements.

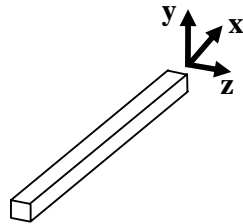


Fig. 5. Beam element local coordinate system

Material properties used in the model were obtained from the material characterization test program for GFRP pultruded bars (item 2.1).

Capacitor weight and critical wind and short-circuit loads for the structural elements and accessories were evaluated by the equations shown in item 2.3 and used in the stress analysis.

Four individual load cases were proposed for this study. The first one, called test load case, was designed to compare test results with finite element predictions. An equivalent concentrated load was applied on the top of the structure, at an angle of 14° with respect to the structure face plane, in order to simulate the distributed critical wind load in such a way that the test rig could be simplified. The structure was also loaded with the capacitor weights, measured before the test. No short-circuit loads were applied in this case. This load case is presented on Fig. 6.

The other three load cases, called load cases 1, 2 and 3, described the loading conditions for worst case scenarios in the event of each one of the three short-circuit accidents (Figs. 2, 3 and 4) acting in conjunction to critical wind loads. The wind loads, in these three cases, are distributed along the

structure members to simulate the real life situation. These are the critical point design load cases for the structure. As an example, load case 1 is presented in Fig. 7.

Static and stability analyses of the structure model were performed for the four load cases.

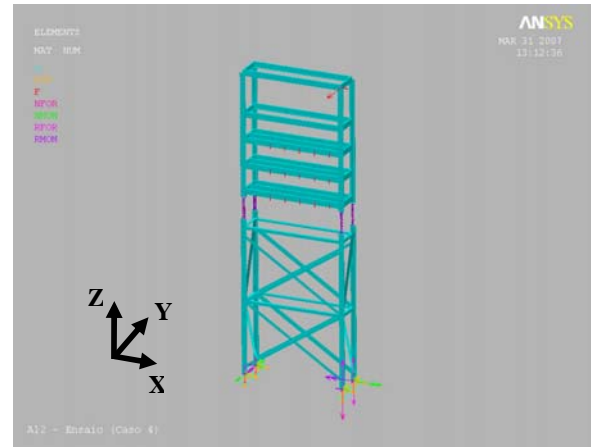


Fig. 6. Test load case

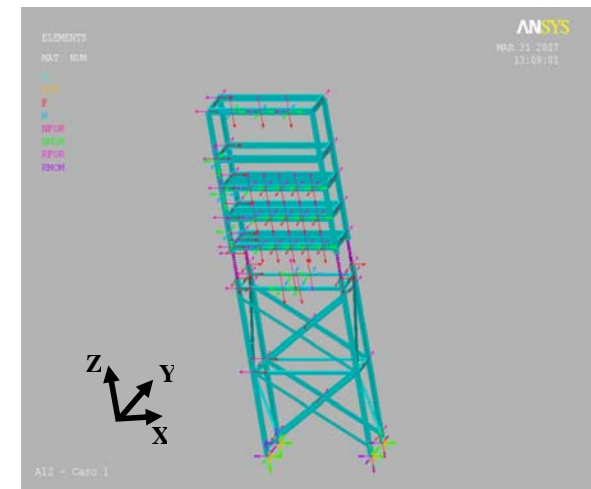


Fig. 7. Load case 1

2.5 Prototype Test Structure

A prototype real scale structure was built to be tested in order to validate the finite element model. This structure, designed according to the imposed requirements, is shown in Fig. 8.

The capacitors were weighted before their installation on the structure, so that their dead load could be fed in the finite element model. The equivalent wind load was applied on the top of the structure through a pulley system attached to an adjacent pole (Fig. 9), with a steel cable pulled by a manually operated ratchet lever hoist (Tirfor). A

load cell was connected to this system in order to measure the applied force.



Fig. 8. Prototype test structure

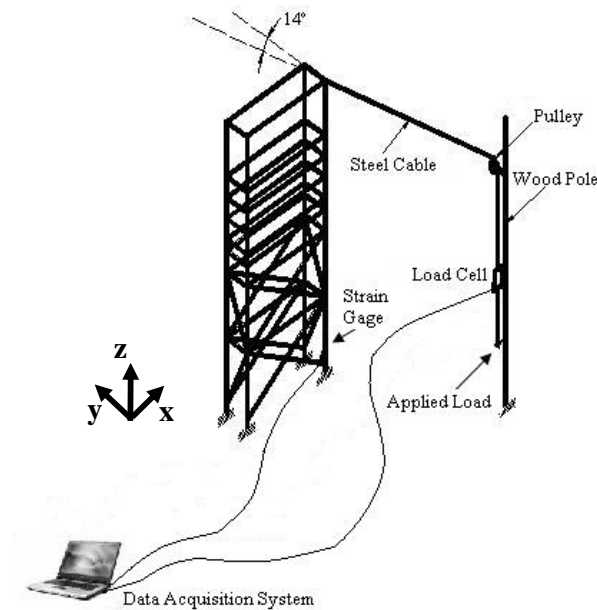


Fig. 9. Prototype test scheme

Eight critical points were selected to be instrumented and monitored with strain gages (Fig. 10), according to results of a preliminary finite element analysis. Axial strain gages were longitudinally attached in the middle of one leg of the L profiles (25.4mm = 1" from the edge), as shown in Fig. 11. Strain gages # 1, 2, 3 and 4 were positioned on the upper bay while strain gages # 5, 6, 7 and 8 were positioned on the lower bay, all of them in points of high strain concentration.,

The load cell and the strain gages were connected to a PC with a data acquisition system shown in Fig. 9 (Agilent Technologies 34970A, accuracy 0.004% and resolution of 6½ digits). During the test, load was continually applied with the data acquisition system recording the synchronized signals from the load cell and from the strain gages.

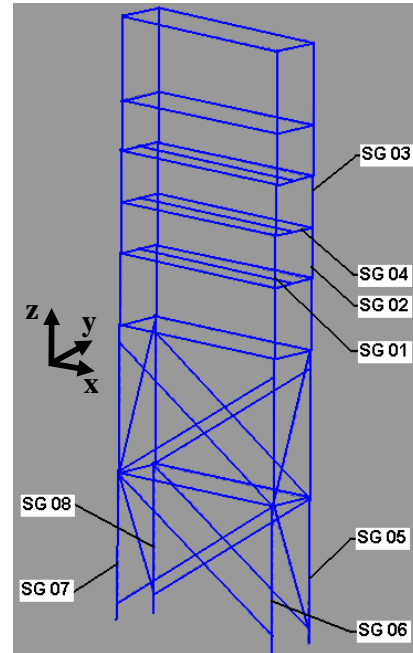


Fig. 10. Strain gage map

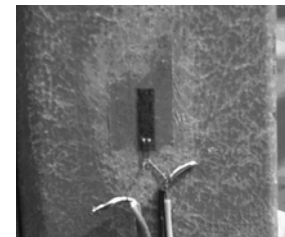
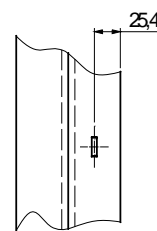


Fig. 11. Detail of strain gage fixation

3 Results and Discussion

3.1 Material Characterization

Results of the material characterization test program are shown in Tab. 1. It can be observed that transverse properties presented lower levels of data dispersion than longitudinal properties. This information was later used in the finite element analysis of the structure.

Table 1. Mechanical properties of the used GFRP

Properties	Unit	Average± STD
Longitudinal Young's Modulus (E_1)	GPa	29.53±1.47
Transverse Young's Modulus (E_2)	GPa	4.49±0.61
Longitudinal Tensile Strength (X_t)	MPa	321.15±13.01
Transverse Tensile Strength (Y_t)	MPa	37.68±1.94
Longitudinal Poison's Ratio (ν_{12})	-	0.33±0.03
Transverse Poison's Ratio (ν_{21})	-	0.06±0.01

3.2 Finite Element Analysis

Finite element analysis was performed for the four selected load cases. Both static stress field and structure stability were evaluated.

Capacitors were weighted and their respective loads applied to the model are presented on Tab. 2 for the fifteen capacitors attached to the structure.

Table 2. Capacitor weight loads in N

Capacitor	1 st	2 nd	3 rd	4 th	5 th
1 st store	479.71	482.65	489.52	498.35	485.60
2 nd store	487.56	487.56	486.58	490.50	502.27
3 rd store	495.41	491.48	491.48	502.27	491.48

The maximum wind load was evaluated as 3127.38 N. This load was distributed along the structure members for load cases 1, 2 and 3.

Short-circuit loads in the Y-direction of the global coordinate system were calculated for load cases 1, 2 and 3, resulting in the applied loads in the busbars for the three electrical phases (A, B and C). These loads are shown in Tab. 3.

Table 3. Busbar short-circuit loads in N

Capacitor	Phase A	Phase B	Phase C
Case 1	119.02	-48.98	-216.98
Case 2	-48.98	287.02	-384.98
Case 3	287.02	-384.98	-48.98

3.2.1 Static analysis

Static analysis was performed for test load case in order to obtain the simulated strain field and compare the monitored point strains to the measurements of the strain-gages. Load vs. strain plots are presented on Figs. 12 to 19, respectively for strain gages number 1 to 8, showing experimental data results compared to finite element model predictions. Results are limited to a load value of

1509.27 N, when the test was interrupted due to system malfunction. Strain measured was very low and, therefore, data is scattered, not presenting the expected linearity. Material was expected to failure with strains around 12% (120,000 μ strain) and plots show maximum strains around 0.03% (300 μ strain). However, it can be seen that model predictions could capture the trend of structure behavior, mainly for the points with higher strain levels.

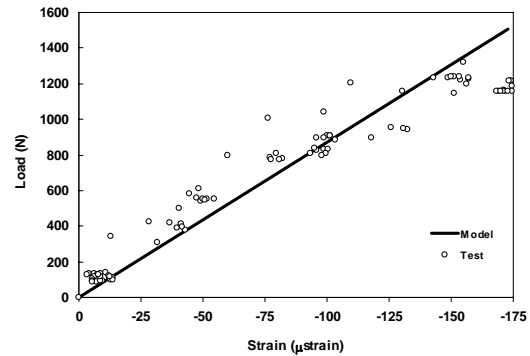


Fig. 12. Results for strain-gage #1

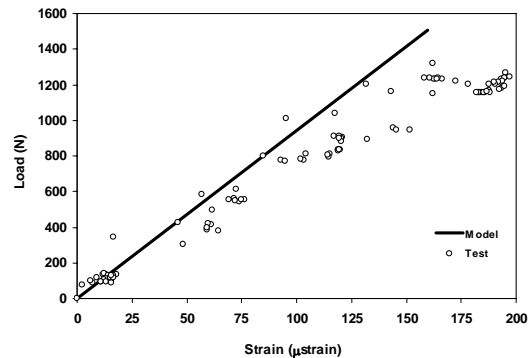


Fig. 13. Results for strain-gage #2

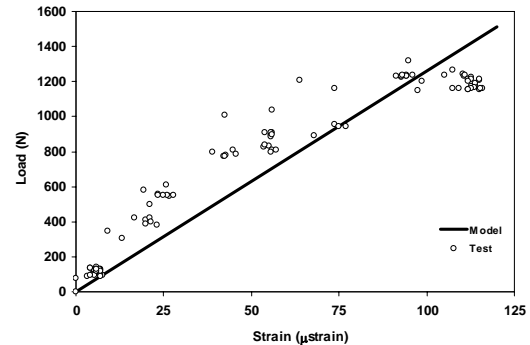


Fig. 14. Results for strain-gage #3

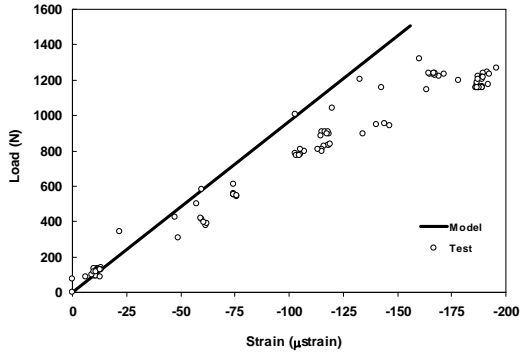


Fig. 15. Results for strain-gage #4

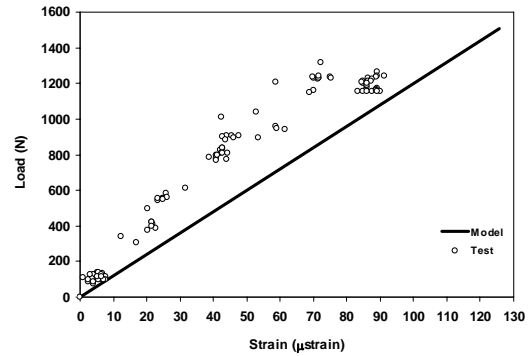


Fig. 19. Results for strain-gage #8

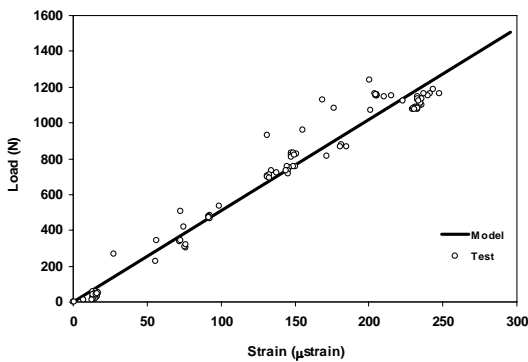


Fig. 16. Results for strain-gage #5

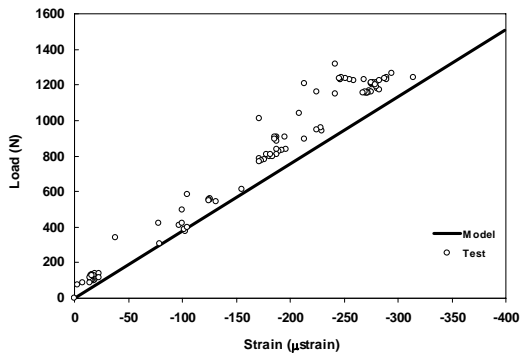


Fig. 17. Results for strain-gage #6

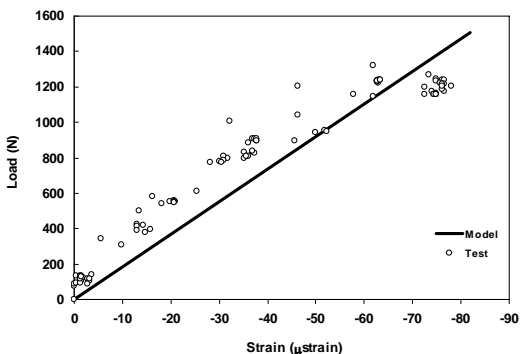


Fig. 18. Results for strain-gage #7

Static analysis for load cases 1, 2 and 3, resulted in the longitudinal stress field respectively shown in Figs. 20, 21 and 22, with maximum tensile stresses of 47.47 MPa, 47.48 MPa and 52.87 MPa. The stresses in the direction of the x-axis of the element local coordinate system, called longitudinal stresses, are presented.

The safety margins (SM) for longitudinal tensile stresses (x-local) were calculated using Eq. 8, and are presented respectively on Tab. 4. It can be observed that the safety margins are all positive and large, indicating that the structure attends well the static requirements.

$$MS = \frac{\sigma_{ult}}{\sigma_{max}} - 1 \quad (8)$$

where:

MS : safety margin;

σ_{ult} : material strength [MPa];

σ_{max} : maximum stress [MPa].

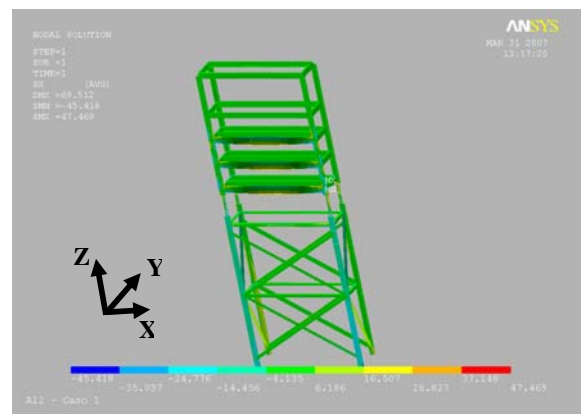


Fig. 20. Longitudinal (x-local) stress field for case 1

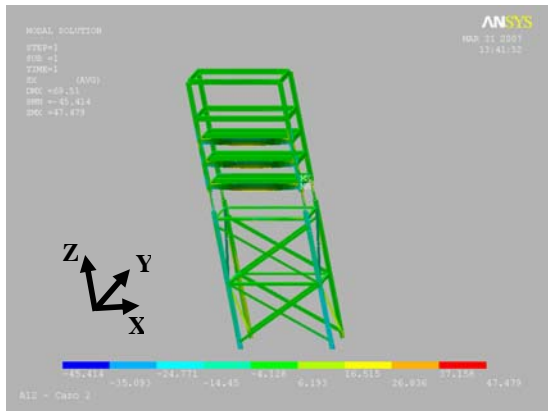


Fig. 21. Longitudinal (x-local) stress field for case 2

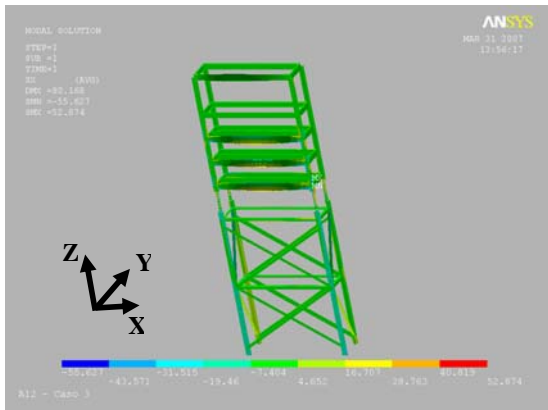


Fig. 22. Longitudinal (x-local) stress field for case 3

Table 4. Safety margins for longitudinal (x-local) tensile stress

Case	σ_{ult} (MPa)	σ_{max} (MPa)	SM
Load case 1	321.15	47.47	5.77
Load case 2	321.15	47.48	5.77
Load case 3	321.15	52.87	5.08

3.2.2 Stability analysis

Buckling structural response for framed structures is very sensitive to boundary conditions imposed to their structural members (bars). Beam elements used in the model are assumed to be perfectly joined. However, in the real structure members are connected through bolted joints. It is clear, then, that boundary conditions for the members of the real structure are somewhere between perfect clamped (all six degrees of freedom of the nodal connection restrained) and perfectly hinged (only the three displacement degrees of freedom of the nodal connection restrained, with the other three angular degrees of freedom allowed). It

is very difficult to access the boundary conditions for members of a real framed structure. This task will highly depend on the stiffness of the members' joints.

Only global buckling failure analysis was performed. The L and U shaped profiles usually undertake local elastic buckling of the leg edges before the global column buckling failure takes place. This effect was not evaluated in this work.

Stability analysis was performed for the three critical load cases. Eigenvalues (λ) for first-bar-to-buckle were determined for each load case. These eigenvalues represent the ratio between the buckling critical failure load (P_{cr}) divided by the actual load in each member (P), as shown in Eq. 9. Results are listed on Tabs. 5, 6 and 7, respectively for first-, second-, and third-bar-to-buckle. The sequence first-, second-, and third-bar-to-buckle was the same for all load cases. This sequence is shown on Figs. 23, 24 and 25, for load case 1, as an example, highlighting the respective buckled bar.

Two different columns of eigenvalues can be seen in Tabs. 5, 6 and 7. They are referred to the two limiting cases of member boundary conditions, respectively clamped (λ_C) and hinged (λ_H), as mentioned before. The finite element analysis resulted in eigenvalues for clamped member boundary conditions (λ_C). Eigenvalues for hinged member boundary conditions (λ_H) were evaluated as $\frac{1}{4}$ of eigenvalues for clamped member boundary conditions (λ_C), using the same theoretical relation as Euler's column buckling theory [9]. The safety margins for clamped and hinged member boundary conditions, respectively SM_{BC} and SM_{BH} , were evaluated according to Eq. 9 and presented on adjacent columns to λ_C and λ_H . These values can be considered, respectively, as upper and lower bounds for the real structure buckling failure safety margins.

$$MS_B = \frac{P_{cr}}{P} - 1 = \lambda - 1 \quad (9)$$

where:

MS_B : buckling failure safety margin;

P_f : buckling critical failure load [N];

P : member load [N];

λ : evaluated eigenvalue (λ_C or λ_H).

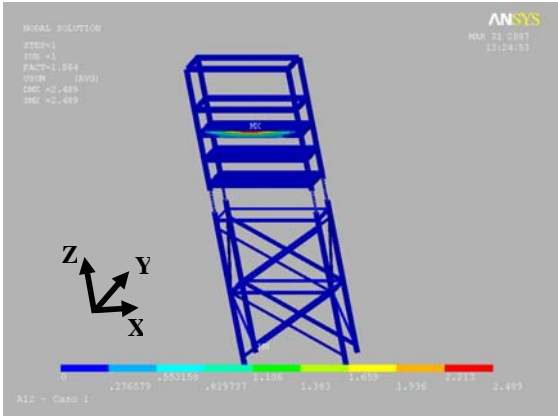


Fig. 23. First bar to buckle for load case 1

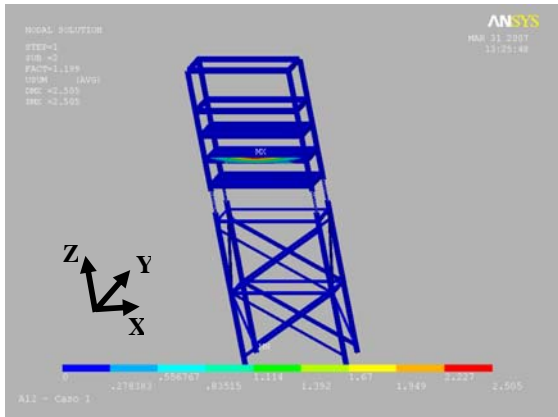


Fig. 24. Second bar to buckle for load case 1

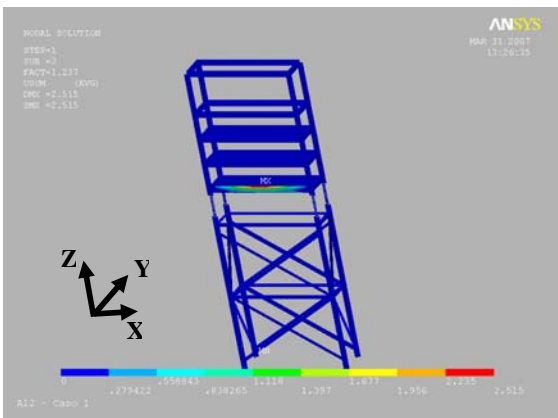


Fig. 25. Third bar to buckle for load case 1

Table 5. Safety margins for first-bar-to-buckle

Load Case	λ_c	SM_{BC}	λ_H	SM_{BH}
Load case 1	1.0843	0.0843	0.2711	-0.7289
Load case 2	1.0843	0.0843	0.2711	-0.7289
Load case 3	1.0707	0.0707	0.2677	-0.7324

Table 6. Safety margins for second-bar-to-buckle

Load Case	λ_c	SM_{BC}	λ_H	SM_{BH}
Load case 1	1,1993	0,1993	0,2998	-0,7002
Load case 2	1,1993	0,1993	0,2998	-0,7002
Load case 3	1,1831	0,1831	0,2958	-0,7042

Table 7. Safety margins for third-bar-to-buckle

Load Case	λ_c	SM_{BC}	λ_H	SM_{BH}
Load case 1	1,2368	0,2368	0,3092	-0,6908
Load case 2	1,2368	0,2368	0,3092	-0,6908
Load case 3	1,2041	0,2041	0,3010	-0,6990

The worst case scenario is load case 3, where structure buckling failure safety margin for first-bar-to-buckling is close to 0.07 (7%) considering clamped member boundary conditions (upper bound) and to -0.73 (-73%) considering hinged member boundary conditions (lower bound). Safety margins are larger but still marginal for second- and third-bar-to-buckle. Although real structure members will have a safety margin between these upper and lower bounds, it is reasonable to assume that the structure is somehow in the verge of failure. Therefore, it is strongly recommended to reinforce critical members which present limiting buckling failure safety margins.

5 Conclusions

This work presented a study on the technical viability for application of pultruded composites bars in capacitor bank framed structures. A finite element model was developed to perform static and stability analysis of the structure. Material properties used in the model were obtained from a material characterization test program. A prototype real-scale test structure was built, instrumented and tested to validate the model. Test was interrupted because of system malfunction, but recorded results were in agreement with model predictions.

Additional three critical load cases were simulated for capacitor weight loads, maximum wind loads and short-circuit loads. Results showed large safety margins for static analysis. However, safety margins for structure global stability were marginal and highly dependent of members' boundary conditions. Therefore, structure reinforcement on specific bars is advised.

In general, results support the use of GFRP as an alternative material in the design of capacitor bank framed structures.

Acknowledgements

The authors would like to acknowledge the contribution of Cristiano C. Vieira, Anderson M. Gomes, Humberto R. Meneses, Beline Q. A. Fonseca, Denis H. B. Scaldasferri and the CEMIG maintenance crew. This work was supported by a grant from the Energy Company CEMIG and the Brazilian Federal Agency of Electrical Energy ANEEL.

References

- [1] Karbhari, V.M. and Zhao, L. "Use of composites for 21st century civil infrastructure", *Journal of Computer Methods in Applied Mechanics and Engineering*, pp 433-454, 1999.
- [2] Paciornik, F.M.S. et al., "Analysis of the mechanical behavior and characterization of pultruded glass fiber – resin matrix composites", *Journal of Composite Science and Technology*, pp 295-304, 2002.
- [3] Mottram, J.T. and Zheng, Y. "State-of-the-art review on the design of beam-to-column connections for pultruded frames", *Journal of Composites Structures*, pp 387-340, 1997.
- [4] ASTM, D 3039. "Standard Test for Tensile Properties of Fiber-Resin Composites", American Society for Testing and Materials, Philadelphia, 1989.
- [5] ABNT, NBR 5422. "Projetos de linhas aéreas de transmissão", Associação Brasileira de Normas Técnicas, Rio de Janeiro, 1985. (In Portuguese).
- [6] Krauss, J.D. and Carver, K.R. "Electromagnetics", 2nd edition, McGraw-Hill, 1973.
- [7] IEEE. "IEEE Guide for Design of Substation Rigid-Bus Structures", The Institute of Electrical and Electronics Engineers, 1998.
- [8] Budinich, M.D. and Trahan R.E. "Dynamic analysis of substation busbar structures", *Journal of Electric Power Systems*, pp 47-53, 1995.
- [9] Popov, E.P. "Resistência dos materiais", 2nd edition, Rio de Janeiro, Prentice-Hall do Brasil 1984. (In Portuguese)